Characterisation of off-axis tensile behaviour and mesoscale deformation of woven carbon-fibre/PEEK using digital image correlation and X-ray computed tomography

John Holmes[a,*], Silvano Sommacal[a], Raj Das[b], Zbigniew Stachurski[c], Paul Compston[a]

[a] *ARC Training Centre for Automated Manufacture of Advanced Composites, Australian National University, Acton, ACT 2601, Australia*
[b] *School of Engineering, Australian National University, Acton, ACT 2601, Australia*
[c] *Aerospace Engineering and Aviation, RMIT University, Melbourne, VIC 3000, Australia*

Abstract

The architectural intricacy of multi-ply woven composites, caused by differences in layer alignment, introduces complexity into their mesoscale response to on- and off-axis tensile loading. To better understand the relationship between architecture and deformation response, this work combines digital image correlation (DIC) and 3D micro-computed tomography (μCT) to examine deformation for 0°, 15°, 30° and 45° specimens. Tensile tests were conducted with a four-layer plain woven carbon/polyetheretherketone (C/PEEK) laminate. In addition to the evident variance of mechanical properties between orientations, significant mesoscale differences in topography and strain were observed resulting from the layer alignment of individual specimens. Alignment of the top two surface layers induced distinct topographical peaks under extension, whereas nested architectures formed continuous topographical ridges. Matching observed surface strains around microstructural cracks identified in μCT images revealed both inter-tow and intra-tow shearing during off-axis extension and corresponding fibre reorientation, which effectively illustrates the potential benefits from combining DIC and μCT.

Keywords: Digital Image Correlation (DIC), micro-Computed Tomography (μCT), Off-axis properties, Surface topography, Woven thermoplastic composite

*Corresponding author
Email addresses: John.Holmes@anu.edu.au (John Holmes), Silvano.Sommacal@anu.edu.au (Silvano Sommacal), raj.das@rmit.edu.au (Raj Das), Zbigniew.Stachurski@anu.edu.au (Zbigniew Stachurski), Paul.Compston@anu.edu.au (Paul Compston)

1. Introduction

Composites with woven fibre architecture and thermoplastic matrices provide manufacturers in the aerospace, automotive, and energy industries a lightweight and rapidly thermo-formable material [1–3]. As a consequence of geometric complexity of manufactured parts, the load pathway is not necessarily aligned with the weave direction. For satisfactory performance prediction, knowledge of the deformation behaviour under on- and off-axis loading is necessary. Moreover, a multi-scale understanding is needed, incorporating both global mechanical response and local mesoscale behaviour. While much work has focused on macroscale mechanical properties, there is also a need to study the local heterogeneity of the mesoscale weave response. The increasing prevalence of advanced characterisation techniques, including digital image correlation (DIC) [4, 5] and micro-computed tomography (μCT) [6–9] provides the method for detailed study of local deformation response and allows insight into deformation mechanisms at the weave level.

The study of off-axis behaviour has been motivated by the significant difference in mechanical properties with directional loading, with knowledge of this anisotropy an important design consideration. For woven composites under tension, increasing the off-axis loading angle from 0° to 45°, increases the strain to failure by a factor of 1.5 to 15 times [10–18], decreases stiffness by a factor of 1.6 to 6.9 [12–14, 16–19] and decreases ultimate strength by a factor of 1.5 to 7.5 [10–17]. The degree of anisotropy in the mechanical response is influenced by the choice of fibre (glass, carbon), matrix (thermoset, thermoplastic), and weave (plain, satin, twill). Carbon fibre composites can have significant differences between on- and off-axis extension due to the low strain to failure of the fibres ($\sim$1.5%) [14, 16]. The ductility of the matrix influences the ability of off-axis fibres to reorientate under load. The choice between thermoset or thermoplastic greatly influences ductility, with strain rate and temperature also influential for the ductility of viscoelastic thermoplastics [16, 17, 20–22]. Differences in the global Poisson's ratio are a consequence of fibre reorientation, varying from 0 to 0.1 for on-axis loading to 0.6 to 1.0 when loaded in the off-axis [12, 14, 19]. Compared to the other factors discussed, the weave style and degree of interlocking have a more moderate impact on the change of macroscopic mechanical properties [19]. However, while the global mechanical response is important for engineering and manufacturing design choices, the mesoscale behaviour of the weave architecture is crucial for understanding local deformation and damage development.

Analysis of the full-field surface strain maps provides insight into the local strain heterogeneity of woven architectures. On-axis studies have found strain concentrations in resin-rich regions between tows and higher strain on transverse surface tows, which are pushed outwards by straightening of the tow under tension beneath them [23–25]. This pattern is closely linked to the weave style (plain, twill, and satin) and loading direction [23, 26–29]. Research into off-axis strain maps has found high strain at tow edges, as shearing of the bridging matrix between them occurs with tows sliding past each other during reorientation [12–14, 27]. In the 45-degree off-axis case, this pattern is relatively symmetrical and most concentrated where both diagonals intersect [22, 26, 30]. Strain variation has been linked to the topographical analysis of the surface deformation for on-axis testing, with higher surface strain and topographical peaks occurring in surface tows transverse to the loading [23, 31]. However, the topographical development during loading and relation to strain map have not been studied in the off-axis case.

The strain map and surface topography are closely related to the underlying weave architecture of the composite. For multi-layered composites, the alignment of internal layers influences the response. Finite element simulations and experimental testing have shown substantial differences in the mesoscale surface strain map [28, 31–33], internal stress and damage distribution [34–36], and more minor differences in macroscale strength and stiffness [32, 36–38]. A higher degree of layer-shifting (nesting) between the woven layers constrains the large surface strain gradients and reduces the distinct pattern linked to the surface tows [31, 39]. These different degrees of nesting have been linked to changes in local damage, including longitudinal and transverse cracking, most significantly in intra-tow regions, and less frequently differences in tow and layer debonding and delamination [13, 40–42]. Higher nesting between layers of woven reinforcement also has an influence on resin impregnation during manufacture by reducing the size of channels for resin flow and hence reducing the permeability [43–45]. The aforementioned studies, have typically focused on simulation or experimental analysis of on-axis properties, with few works concerned with reporting experimental results for off-axis behaviour. Moreover, existing work has commonly used microscopy slices through the material, which cannot thoroughly elucidate the 3D architectural morphology. The capabilities of modern micro-computed tomography (μCT) now provide a tool for a detailed 3D examination of weave architecture and have been effectively used to examine composite damage development [7, 8] and improve the accuracy of mesoscale simulations [6]. Further experimental work is needed to link the 3D internal microstructure to observed surface strain and topographical development to allow the variability in surface observations to be better related to the underlying weave morphology.

In this paper, the on- and off-axis strain maps of a high-performance carbon fibre polyetheretherketone composite are characterised under tensile load and related to surface topographical change. This novel experimental investigation determines the influence of weave layer-shifts, from μCT, on topography and strain contour variability, from DIC, under on- and off-axis loading. The findings presented relate variations in the internal microstructure with observed mesoscale strain and topography changes. These insights provide a valuable resource for predicting internal architectural alignment from observed surface deformation, beneficial in understanding and simulating damage and deformation of multi-layered woven composites.

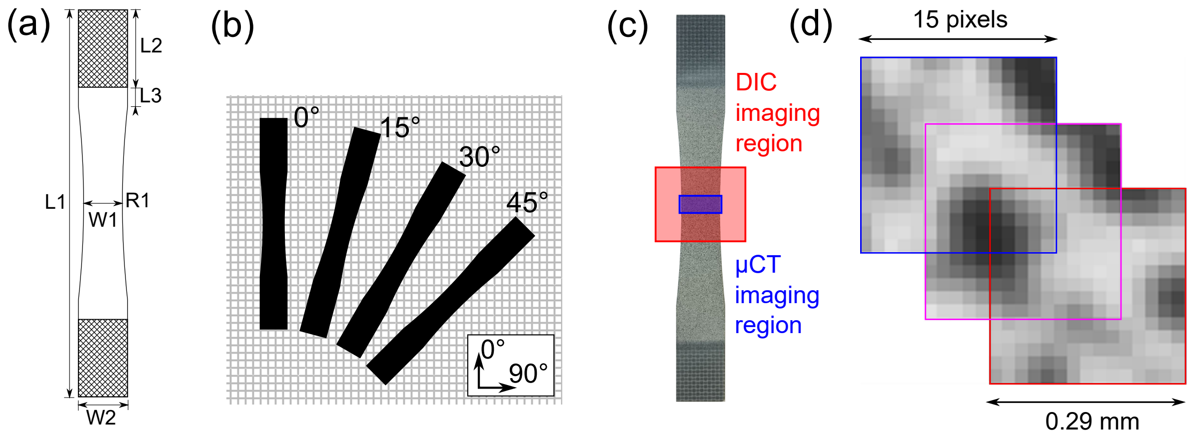

Figure 1: Specimen design, (a) geometry of tensile specimen: L1 = 200, L2 = 40, L3 = 10, W1 = 20, W2 = 25.4, R1 = 464.31 (in mm, L = length, W = width, R = radius), (b) specimen orientations 0°, 15°, 30° and 45°, (c) painted specimen with region of interest for DIC and μCT imaging, and (d) DIC overlapping pixel subsets with painted pattern.

2. Experimental method

2.1. Material

The material used in this study is a four-layer plain woven carbon fibre / polyetheretherketone matrix (C/PEEK) laminate. It is made from Pipreg® from Porcher Industries with powder impregnation and a double belt press for consolidation. Tow spacing is ∼2 mm, and the laminate has a thickness of 1 mm with a 50% fibre volume fraction. The microstructure of the material varies as the random shifting between pairs of layers during manufacture can result in aligned, nested or balanced architecture for each sheet consolidated.

2.2. Specimen design

The specimen design in Figure 1a is commonly used for tensile testing of woven composites [46–48]. It has a maximum width of 25.4 mm, to suit the grips, and a length of 200 mm, with the additional dimensions specified in Figure 1a. Specimens were cut using a waterjet at 15° angle increments from the primary 0° direction up to 45°. Figure 1b illustrates specimen orientations, but individual specimens of different orientations were cut from separate sheets to have independent microstructures. The curved specimen design is advantageous in concentrating strain and damage in a small region for observation, and the wider end sections prevent failure in the grips, eliminating the need for gluing additional tabs to the specimen. However, for characterising mechanical properties which required a constant cross-sectional area throughout the specimen length, additional rectangular specimens of constant 20 mm width for the 200 mm length were used for testing.

2.3. Tensile testing

Tensile testing was conducted on a hydraulic 25 kN INSTRON® (model 8874) at a rate of 2 mm/min until failure. The ends of the specimens were clamped using hydraulic wedge action grips (model 8260C) with serrated 25.4 mm by 40 mm faces (model 2703-801), as shown by the hatched region in Figure 1a. A stereo DIC system (ARAMIS® version 6.3) was positioned facing the tested specimen to capture surface displacement and strains. Figure 1c shows the random black and white paint pattern covering the gauge region sprayed onto the specimens before testing. The measuring volume was set to 45 mm by 40 mm with a depth of 25 mm, providing high accuracy displacement and strain measurement while capturing multiple unit cells of the weave.

The cameras have sensors of 2448 by 2048 pixels, which results in a magnification of approximately 51 pixels/mm. Points were found by correlating 15 by 15 pixels (290 μm) subsets and points were generated every 5 pixels (95 μm), illustrated in Figure 1d. The random error in the displacements was determined from an initial series of unloaded images for each specimen, as described in previous works [23, 49], and was found to be on average ± 0.29 μm for in-plane and ± 1.35 μm for out-of-plane displacements respectively. The local strain accuracy was similarly determined and was found to be $\pm 0.17\%$ for ϵ_x and ϵ_y and $\pm 0.14\%$ for ϵ_{xy}. Data points were then exported to MATLAB® for visualisation and topographical analysis. Additionally, a central region of each specimen, 8 mm high, was cut using a diamond saw (Leco VC50) across the whole specimen width, for μCT imaging (Figure 1c).

2.4. Topographical analysis

The local surface topography of woven composites changes when specimens are extended and can be quantified from DIC data. The topographical change is caused by straightening of fibres in the direction of loading under applied extension, which forces transverse fibre bundles above them out of the surface and generates topographic peaks, as shown for specimen $S1_0$ in Figure 2a. A previously developed technique [23] is used in this work to isolate the local change in weave height, Z_{change}, from the global specimen motion. The technique uses fitted surfaces to remove the global out-of-plane motion and leave the small local out-of-plane deformation for each point compared to the fitted surface (Figure 2b). The 95% interval peak to valley topographical height provides a single metric representing the extent of the topographical change. This metric is used to compare individual specimens and results from different directions of extension, limiting the influence of outliers from variation in the DIC measurements.

2.5. X-ray CT analysis

X-ray micro-computed tomography (μCT) enabled the layer alignment of the internal weave architecture to be characterised in 3D. Scanned volumes were acquired from a horizontal cut central

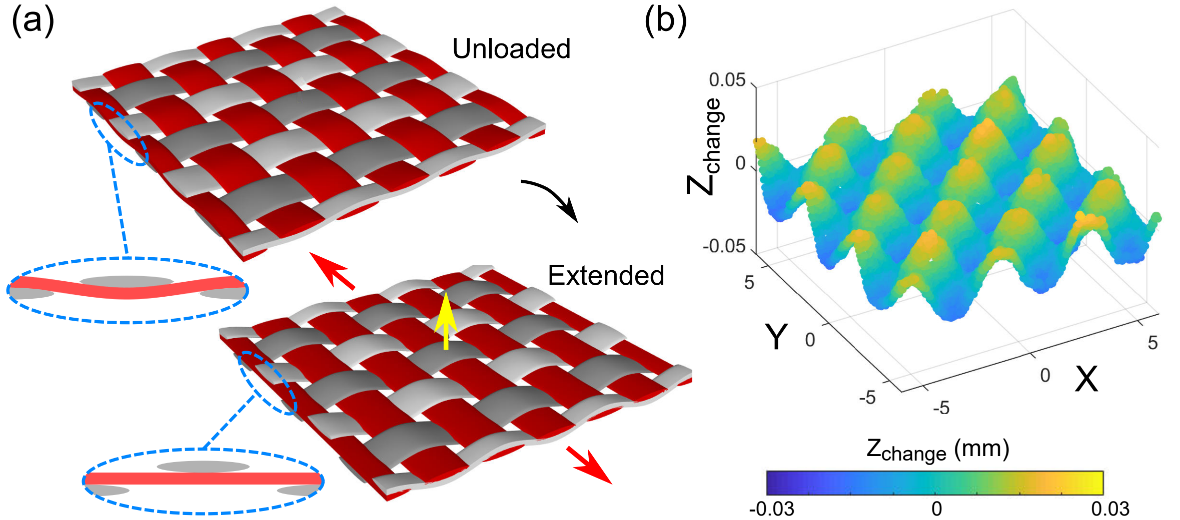

Figure 2: Architectural mechanism of topographical change, (a) straightening of fibre tows under applied extension (red) cause transverse tows (grey) to be pushed outward from the surface, (b) Z_{change} topography on the surface corresponding to architectural change from extension.

section of each specimen, rotated vertically for imaging. Specimens were imaged using a HeliScan^{TM} micro-CT instrument hosted at the ANU CTLab, equipped with a micro-focus X-ray source of 60 kV [50]. Specimens, scanned in stacked pairs, were mounted on a rotating stage with 3600 radioscope projections acquired during each 360-degree rotation interval of the helical imaging path, with a total 14000-18000 projections for the complete imaged helix of each specimen pair. The corresponding acquisition time for each specimen pair was between 21 and 25 hours. The acquired 2D projections, each with a size of 3040 by 3040 pixels, were then reconstructed into 3D grey-scale 16-bit volumes, see Figure 3a, at a scanning resolution of 4.2 µm/voxel using a proprietary ANU reconstruction algorithm [51].

The tomograms then underwent additional image processing for qualitative and quantitative analysis and 3D visualisation, including image segmentation of fibres bundles and matrix using the Mango software tool [52]. Before segmentation, the low intensity contrast between carbon fibre and PEEK matrix was enhanced by applying a proprietary denoise filter on the original tomogram image based on the Non-Local Means algorithm, which resulted in distinct peaks for the two phases, as shown in Figure 3b. Image segmentation was subsequently carried out in Mango using the technique described in [52]. The segmentation method combines grey-scale intensity, gradient, and surface morphology, and uses a bottom-up watershed filling scheme [53]. The resulting segmentation was used to mask the matrix and voids of the original image, see Figure 3c, while preserving the original texture for subsequent fibre analysis. Fibre orientation analysis and visualisation were conducted using the Fiji (ImageJ) plugin OrientationJ [54]. OrientationJ relies on the gradient structure tensor in a local neigh-

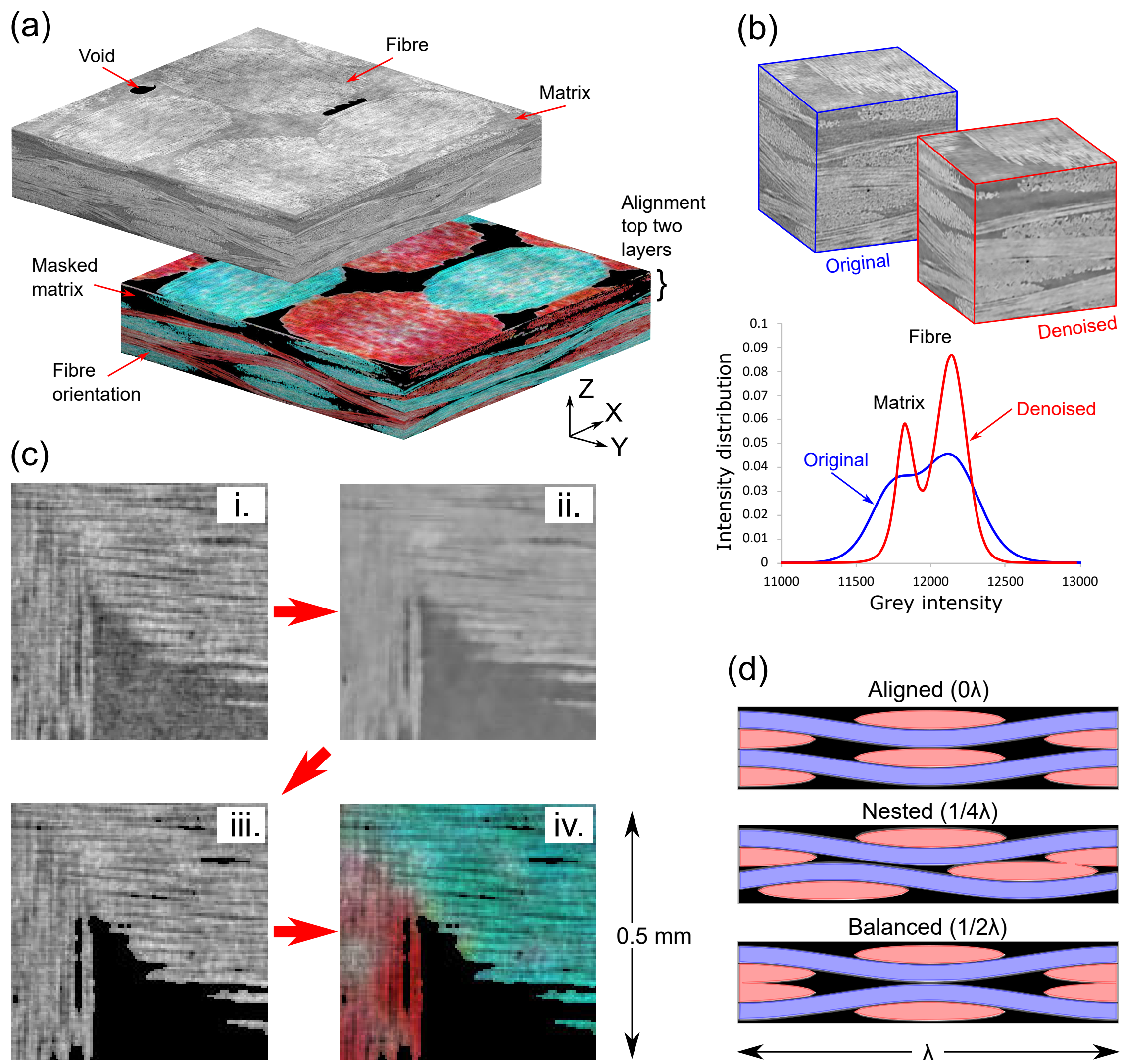

Figure 3: Architectural characterisation, (a) μCT tomogram image for a woven unit cell (4.2 x 4.2 x 1 mm) (top) and with matrix and voids masked and in-plane fibre directions identified, (b) grey-scale histograms for a small volume, original and denoised, demonstrating that fibre and matrix grey levels become more distinct in the denoised image, (c) i. original volume slice, ii. denoised slice for segmentation, iii. original slice with segmented matrix masked, iv. masked slice with overlaid fibre orientations, (d) illustration of types of layer shifts, expressed in terms of λ, between the top two layers.

bourhood and can therefore detect the fibre orientation within the tows even when fibres cannot be tracked individually, as is evident in Figure 3c. A local window of 5 voxels (21 μm) and a cubic spline gradient were used for the structure tensor.

Fibre orientation for the 3D volume, as shown in Figure 3a, then allowed for analysis of woven architecture, including layer alignment. Previous work indicates that the alignment of the top two layers is most influential on surface topography and strain, with lower layers having a greatly diminished influence [29, 31]. Therefore, the focus of this work is on the alignment of these two layers, which can be classified as either aligned, nested, or balanced depending on the shifting between them as illustrated in Figure 3d. Layer shifts in the two weave directions are specified in terms of a fraction of the weave wavelength (λ).

3. Results and discussion

3.1. Tensile properties

The mechanical properties of the specimens, determining the behaviour under loading, show significant variation under off-axis tensile loading. The load extension curves in Figure 4a show decreasing maximum load and increasing extension with increasing off-axis loading angle. This trend is mirrored by the stress-strain plots in Figure 4b of the central region of the specimen. There is increasing non-linearity prior to failure for off-axis loading, with literature suggesting this non-linearity starts between 5° and 10° [10]. The non-linearity is evident for 15° and becomes more pronounced in the 30° and 45° specimens with a shallow slope during the shear dominated deformation. The differences with increasing loading angle translate into differences in multiple tensile properties in Table 1 with a decrease of maximum stress of 2 times, an elastic modulus decrease of almost 4 times, an increase in absorbed energy by 5 times, and an almost 12 times increase in failure strain. This behaviour is intrinsic to off-axis loading of woven composites and is driven by fibre reorientation, with these results characteristic of the findings for woven composites (see ranges of mechanical properties in section 1). A consequence of this increasing fibre reorientation for off-axis specimens is that the ratio of transverse strain (ϵ_x) to strain aligned with the loading direction (ϵ_y) increases. Surface strain aligned with the fibre direction has been investigated as a failure metric in the past for other woven thermoplastic composites [29, 55]. These results for C/PEEK similarly show that with significant shear, as is the case for off-axis specimens, fibre strain decreases, meaning that shear must be taken into account when developing any metric based on surface fibre strain.

3.2. Fibre orientation

In-plane fibre orientation provides insight into fibre distribution and reorientation caused by specimen extension. Fibre orientation obtained from μCT image analysis in Figure 5a shows two distinct peaks corresponding to the four specimen loading orientations. DIC results of these specimens under maximum extension before failure show increasing angular change between warp and weft tows with off-axis loading. While the average angle of all 0° specimens is $90.02 \pm 0.05°$ indicating no detectable change, off-axis specimens show greater transformation: 15° specimens average is $83.71 \pm 0.76°$, 30° is $77.62 \pm 0.55°$, and 45° is $75.13 \pm 1.28°$. These differences in orientation remain visible after testing,

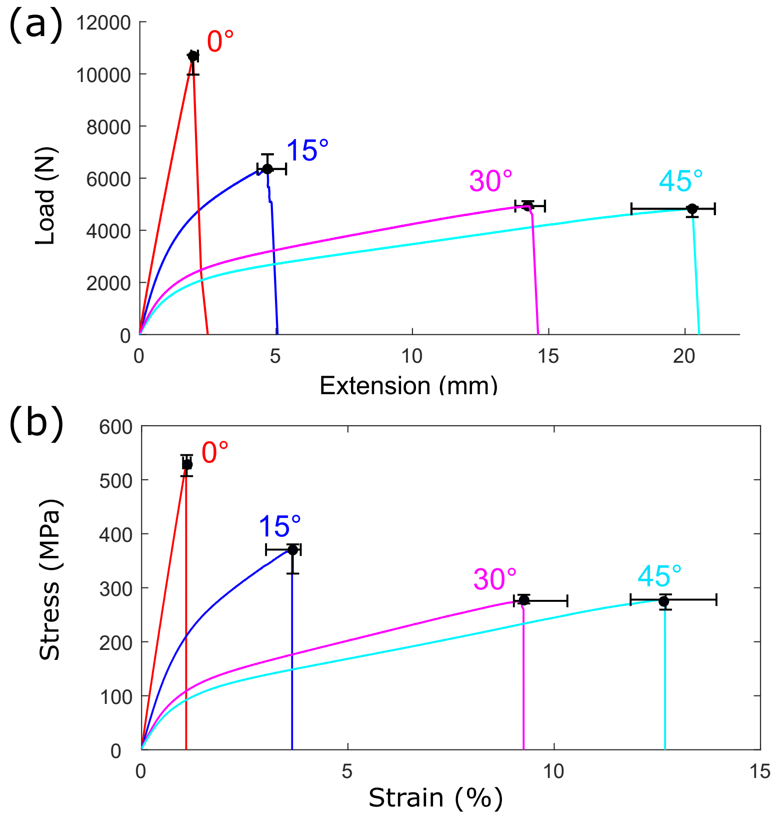

Figure 4: Load response, (a) Load-extension plots for 0°, 15°, 30° and 45° with errorbars based on maximum load and corresponding extension of repeat specimens from INSTRON data, (b) Stress-strain plots at the narrowest region of the specimen using INSTRON load data and DIC strain data from a gauge length of 10 mm.

Table 1: Tensile properties of laminate under directional loading

Loading angle	**0°**	**15°**	**30°**	**45°**
Maximum stress (MPa)[a]	526 ± 19.5	344 ± 17.3	279 ± 8.04	273 ± 14.1
Elastic modulus E (GPa)[a]	46.8 ± 1.37	25.8 ± 1.11	14.6 ± 0.38	12.1 ± 0.59
Absorbed energy (Nm)[a]	12.9 ± 0.98	23.9 ± 3.26	52.4 ± 2.72	65.9 ± 7.56
Failure strain (ϵ_f) (%)[b]	1.098 ± 0.092	3.436 ± 0.421	9.671 ± 0.648	12.892 ± 1.039
Ratio $-\epsilon_x/\epsilon_y$[b]	0.085 ± 0.029	0.796 ± 0.018	1.037 ± 0.057	1.083 ± 0.030
Surface fibre strain (%)[b,c]	1.098 ± 0.092	0.617 ± 0.152	0.443 ± 0.306	0.364 ± 0.103

[a] Mechanical property measured from rectangular specimen geometry, [b] Mechanical property measured from central region of specified specimen design in Figure 1, [c] Measurements from gauge length of approximately 15 mm aligned with fibre angle, noting that for 0 degrees this corresponds to the global direction.

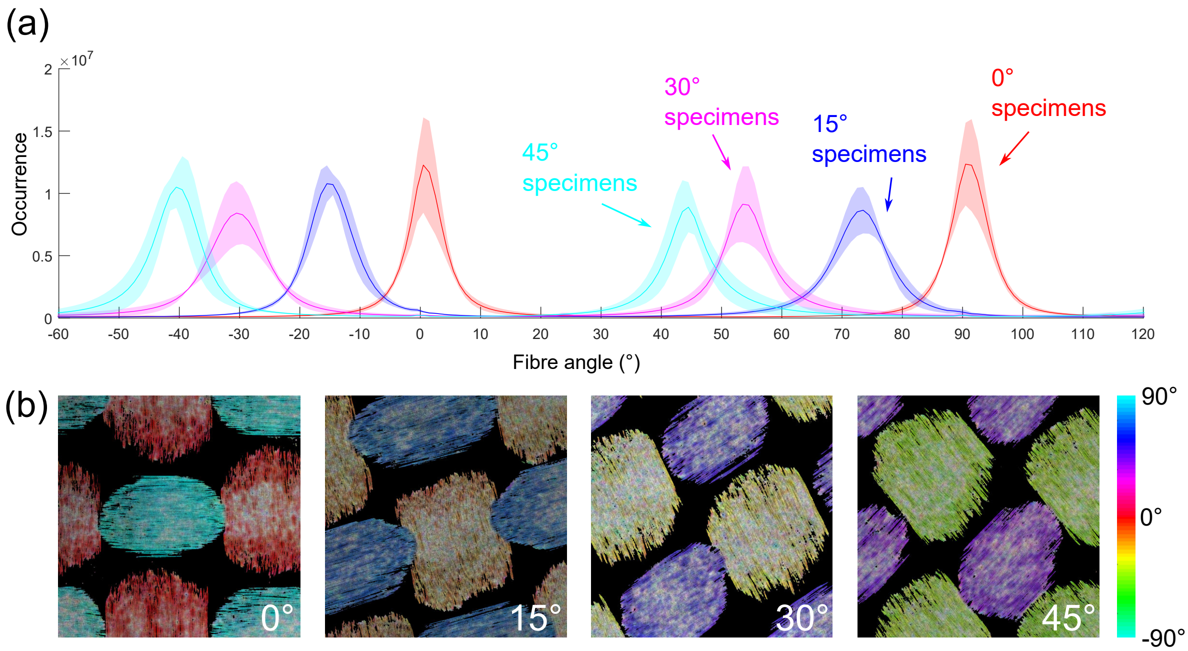

Figure 5: Fibre orientation for on- and off-axis loading, (a) occurrence distribution of fibre orientation versus angle with mean and standard deviation of 3 repeat specimens (colours refer to the loading directions), and (b) representative 2D X-Y tomogram images with fibre orientation for 4.2 by 4.2 mm regions.

despite a partial deformation recovery from unloading and cutting the specimens for imaging. μCT images and surface orientation measurements show that the 0° specimen has orthogonal fibres at ∼90°, whereas 15° specimens have ∼88° fibres, 30° specimens have ∼84° fibres and 45° specimens have ∼82° fibres. The angle changes for the off-axis specimens after loading are about half that of the DIC results during maximum extension, indicating significant recovery driven by the thermoplastic matrix. 2D visualisation of representative μCT slices in Figure 5b shows the local detected fibre orientations for each loading direction. Image artefacts caused by the high density paint results in some noise in the form of speckling within the fibre orientation measurements, but this does not obscure the clear distinction between warp and weft tows and the subsequent 3D visualisation of layer alignment.

3.3. Loading angle topography and strain

Tests for 0°, 15°, 30° and 45° extension directions show different behaviour of the mesoscale strain map and local topography. Significantly, individual specimens also differ based on the alignment of the layers of the weave. These differences are highlighted by the coupled μCT and DIC investigation for three different specimens of each loading orientation. Figure 6 illustrates the relative layer shifts between layer pairs for all specimens. The unique pattern of direction 1 and 2 shifts for each specimen is a consequence of layer shifts varying between the independent consolidate sheets from which every

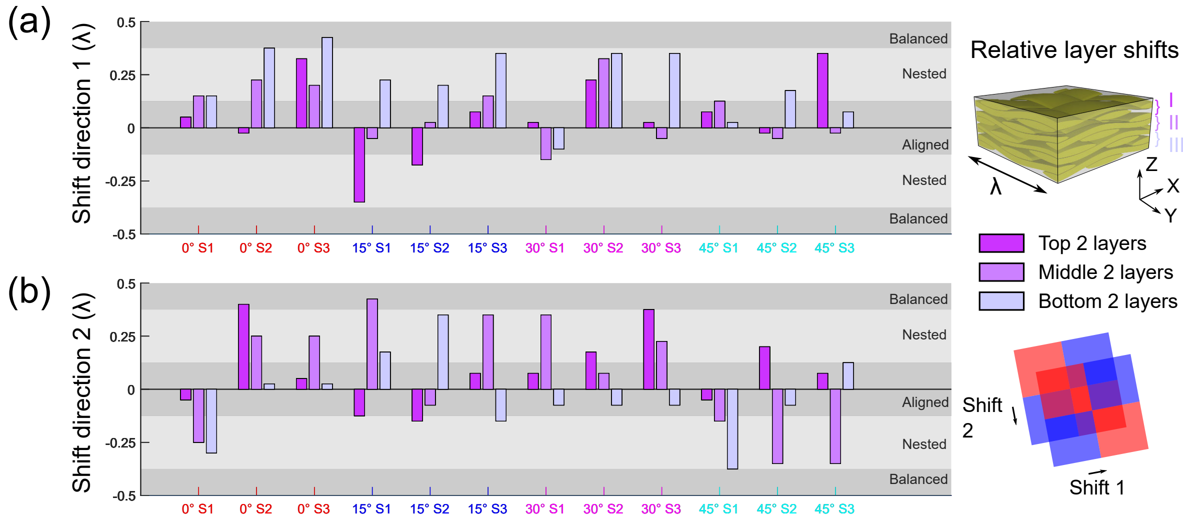

Figure 6: Relative layer shifts between layers for unit cell, (a) layer shift as fraction of wavelength (λ) in direction 1, (b) layer shift as fraction of wavelength (λ) in direction 2. Directions 1 and 2 correspond to X and Y direction for 0° orientation and are rotated counterclockwise in increments of 15° to align with other weave orientations. Negative values indicate that the smallest total unit cell shift is opposite to the direction in the figure.

specimen was cut. The layer shifts between the top two layers greatly influence the full-field strain and topography and are the focus of the following discussion.

The on-axis 0° specimens during extension, Figure 7a, shows the influence of weave alignment. For $S1_0$, the top two layers are closely aligned $< 0.1\lambda$ shift in both 1 and 2 directions. For $S2_0$ the top two layers are balanced, and $S3_0$ is also approaching balanced architecture but has partial nesting (see Figure 6). However, the architecture behaves differently under loading. For $S1_0$, as the fibres in the Y direction (red) straighten, the transverse fibres (blue) are pushed upwards with the weave layer below moving in conjunction, hence providing little resistance. In contrast, the balanced architecture of $S2_0$, means that the layer below directly resists the outward motion of the top weave layer. The slight direction 1 nesting of the top two layers of $S3_0$, reduces the resistance of the weave to motion but not to the extent of $S2_0$. The results of this architecture are evident in the topography contours (Figure 7b), with the peak to valley height 29.1 μm, 13.0 μm, and 15.2 μm for S1 to S3, respectively. Whilst the mean values of strain remain fairly similar (Figure 7c), the standard deviation varies with the same trend as the topography S1 1.18 $\pm$ 0.52, S2 1.04 $\pm$ 0.24, and S3 1.08 $\pm$ 0.27. The primary contributor to the overall major principal strain is ϵ_y, in comparison to ϵ_x and ϵ_{xy}, and the highest strain is associated with the high topographical regions as they are pushed upwards and spread out (Supplementary figure 1).

Off-axis 15° extension similarly shows differences in both the topography and strain, which have links to the internal architecture shown in Figure 8. The alignment of the top two layers is approaching

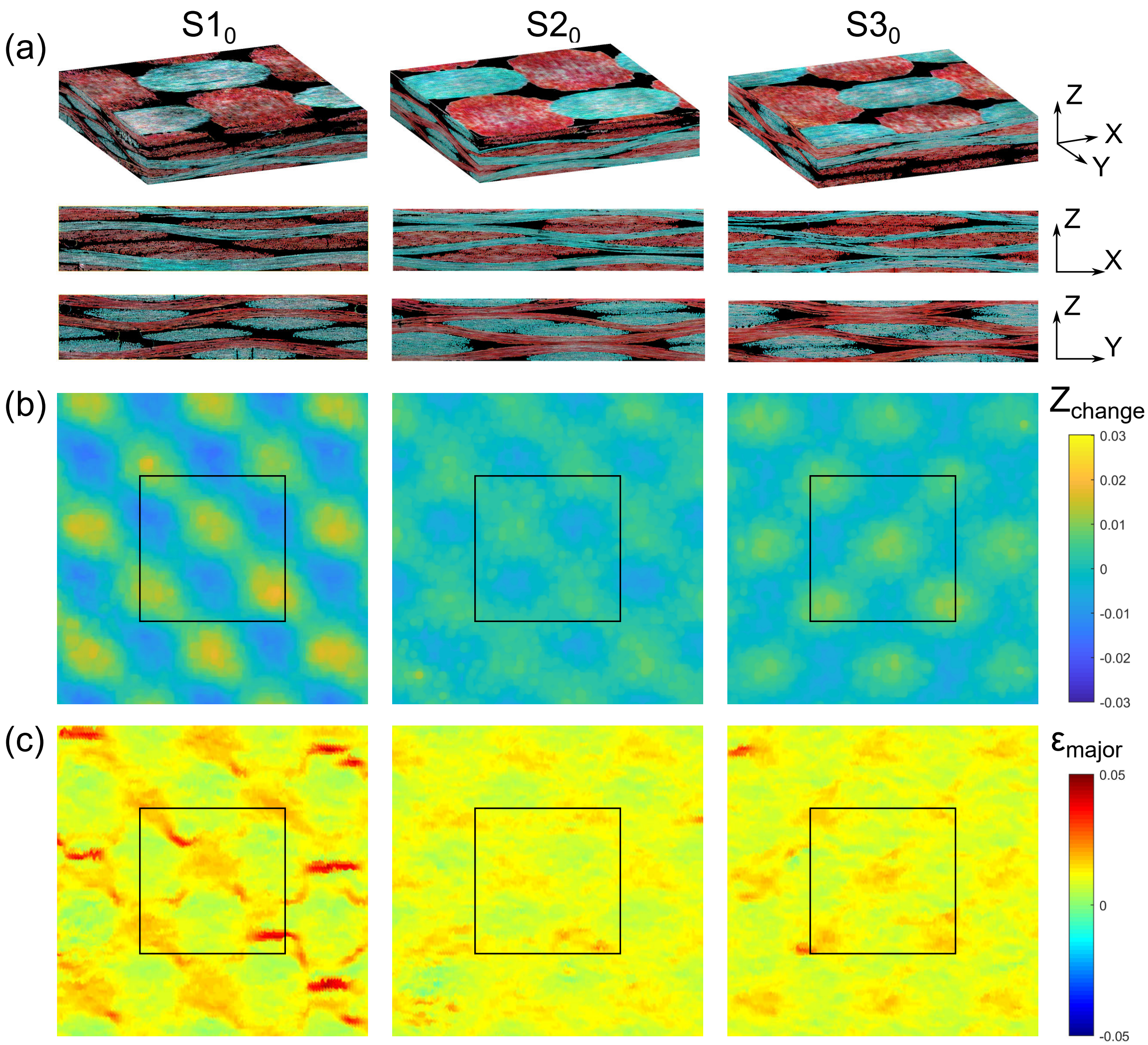

Figure 7: On-axis 0° orientation, (a) fibre orientation architecture for specimens $S1_0$, $S2_0$, and $S3_0$ showing volumetric view (4.2 x 4.2 x 1 mm), XZ, and YZ cross-sections (resin masked to black) of μCT volume, (b) surface topography (Z_{change}) from DIC, (c) major principal strain (ϵ_{major}) for region corresponding to topography and architecture; black box in (b) and (c) shows location of corresponding μCT volume. Additional strain plots in Supplementary figure 1.

balanced for $S1_{15}$, clearly nested for $S2_{15}$, and nearly aligned for $S3_{15}$ (see Figure 6). The topography of $S1_{15}$ and $S3_{15}$ shows discrete topographical peaks compared to the long ridges of the nested $S2_{15}$. The ridges are caused by the second layer pushing upwards in locations where there would otherwise be gaps between the top weave layer peaks. The more significant deformation of the off-axis loading, and underlying fibre reorientation, also results in a greater topographical change with a mean peak to valley height of 33.2 μm compared to 18.7 μm for on-axis. Differences in strains are also evidently linked to architecture. The nesting of $S2_{15}$ contributes to the most uniform strain map, 6.81 $\pm$ 0.89%, while the most aligned $S3_{15}$ has the most variation, 5.61 ± 1.88%, and the balanced $S1_{15}$ is in between the two extremes, 5.92 ± 1.11%. The primary contributors to the difference in major principal strain are differences in the concentration of ϵ_{xy} (Supplementary figure 2). Shear strain is a product of tow intra- and inter-tow fibre sliding under off-axis extension. For 15° specimens, nesting suppresses inter-tow shear concentration, leading to more shear within the tows themselves. These results show that differences in the mesoscale architecture influence the mechanism of off-axis extension, and may be of interest for more detailed study and modelling of microscale and mesoscale damage mechanisms.

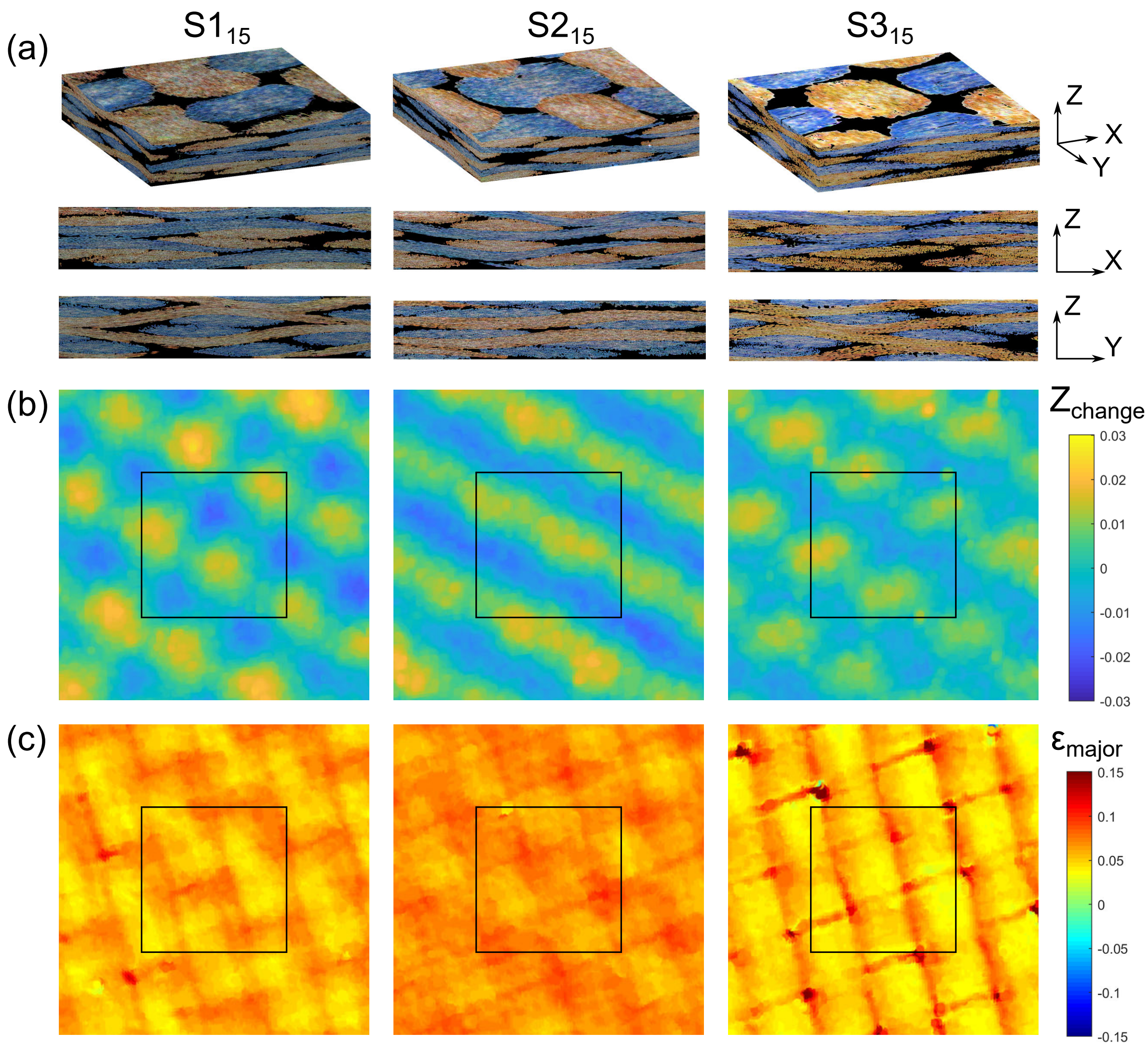

Figure 8: Off-axis 15° orientation, (a) fibre orientation architecture for specimens $S1_{15}$, $S2_{15}$, and $S3_{15}$ showing volumetric view (4.2 x 4.2 x 1 mm), XZ, and YZ cross-sections (resin masked to black) of μCT volume, (b) surface topography (Z_{change}) from DIC, (c) major principal strain (ϵ_{major}) for region corresponding to topography and architecture; black box in (b) and (c) shows location of corresponding μCT volume. Additional strain plots in Supplementary figure 2.

Off-axis 30° testing, Figure 9, shows variation between specimens and also within a single specimen in terms of consistency of topographical and strain features. This inconsistency is a consequence of the larger deformation and fibre reorientation than the 0° and 15° specimens, but it can still be related to the internal microstructure. $S1_{30}$ shows a high degree of alignment of the top two layers, whereas $S2_{30}$ and $S3_{30}$ have significant layer nesting and approaching balanced architecture, respectively (see Figure 6). The aligned $S1_{30}$ has individual topographical peaks corresponding to the synchronous motion of the 60° transverse tows. In contrast, the nesting of $S2_{30}$ and $S3_{30}$ causes irregularity of the surface. A greater degree of local damage and hence more localised topographical variation is evident in $S2_{30}$ compared to the more gradual change in $S3_{30}$. The average peak to valley height is 39.1 μm which, like the 15° specimens, is greater than for on-axis testing. Along with topography, variance in strain, caused by larger deformation and greater reorientation, is more than in 0° and 15° specimens. This variance is highest for $S2_{30}$ (11.81 ± 3.65 %), but also present for $S1_{30}$ (13.44 ± 1.93 %) and $S3_{30}$ (10.61 ± 2.13 %). The regions of higher major strain visible in Figure 9c are contributed primarily by concentration of ϵ_y and ϵ_{xy} between tows (Supplementary figure 3).

Off-axis 45° specimens, in Figure 10, are similar to 30° specimens in showing variation within single specimens as well as between them. Under load, they have the greatest fibre reorientation, and consequently, local variations in the structure have a pronounced influence on the strain and topographical response. The architecture of $S1_{45}$ is close to aligned, while $S2_{45}$ is nested, and $S3_{45}$ is partially nested approaching balanced (see Figure 6). In contrast to the 0° and 15° specimens, high topographical features are associated with high strains and tow edges. Due to the large deformation, matrix extrusion occurs between tows, which has been previously observed in 45° testing [12, 14] but until now, not quantified for the full field surface. Deeper isolated resin pockets for the aligned $S1_{45}$ cause localised matrix extrusion compared to the ridges for the nested $S2_{45}$ and $S3_{45}$. As with other off-axis extensions, fibre reorientation results in a high mean value of topography, 31.5 μm. The strain also exhibits a high degree of variation within the specimens, $S1_{45}$ 11.81 ± 2.94 %, $S2_{45}$ 12.66 ± 2.01 % and $S3_{45}$ 14.39 ± 3.81 %. Strain concentrations between tows are evident, in the case of $S2_{45}$ and $S3_{45}$ predominantly on the perpendicular diagonal to topography (see also Supplementary figures 4). This orientation suggests that more of the shifting and extension is in this direction, causing the tow gaps, transverse to it, to have greater deformation and, hence, topographic change.

The results presented in this section for the mesoscale topography and strain at different loading orientations are useful, considering the increase of engineered structural, semi-structural and interior composite parts in the aerospace and automotive sectors [1, 6]. A better understanding of the relationship between architecture and mesoscale deformation is not only useful for predicting the loaded response but also the behaviour during thermo-forming. For example, woven fibre-reinforced thermoplastic composites are used in commercial aerospace interiors for complex shapes such as overhead

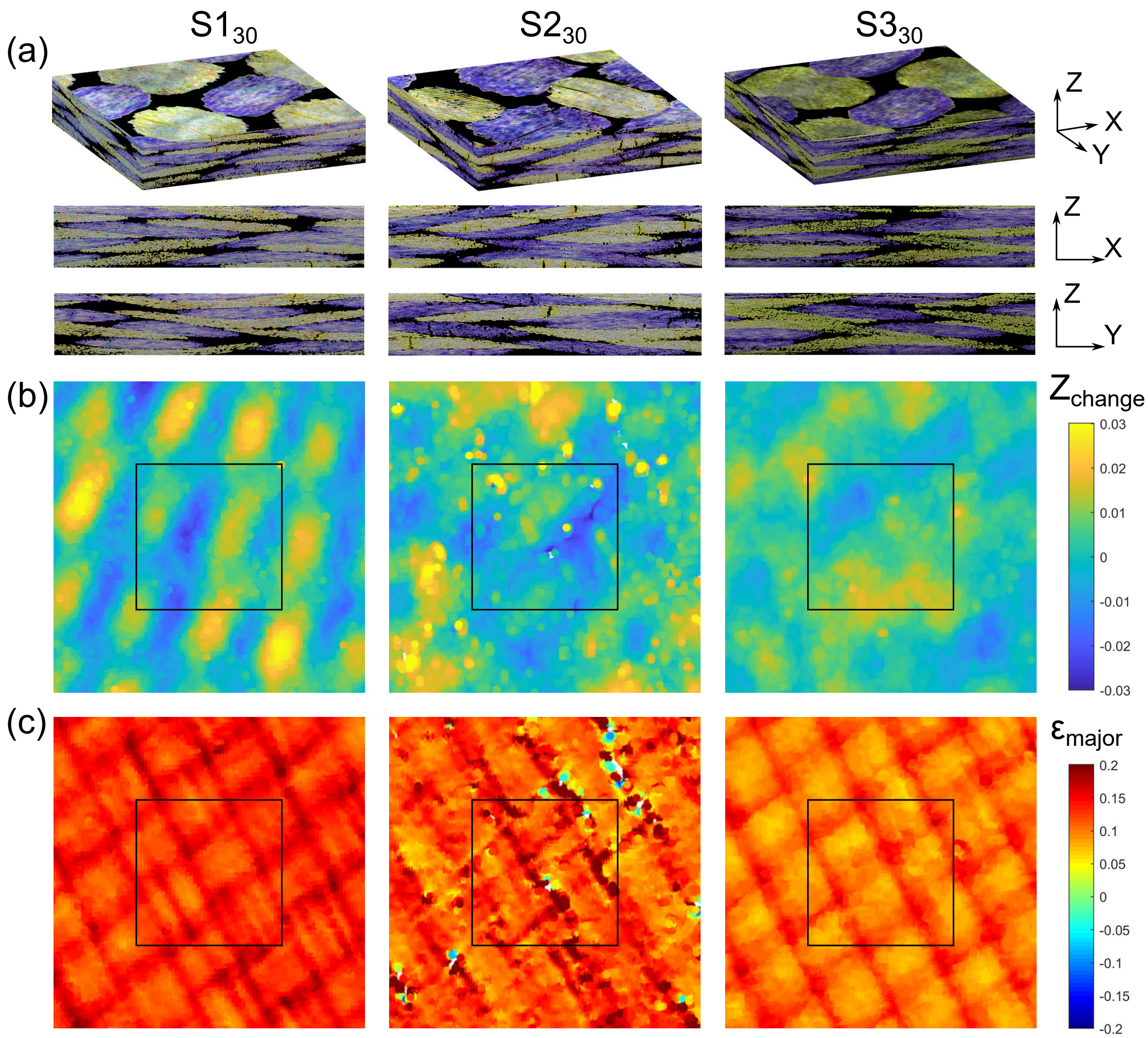

Figure 9: Off-axis 30° orientation, (a) fibre orientation architecture for specimens $S1_{30}$, $S2_{30}$, and $S3_{30}$ showing volumetric view (4.2 x 4.2 x 1 mm), XZ, and YZ cross-sections (resin masked to black) of μCT volume, (b) surface topography (Z_{change}) from DIC, (c) major principal strain (ϵ_{major}) for region corresponding to topography and architecture; black box in (b) and (c) shows location of corresponding μCT volume. Additional strain plots in Supplementary figure 3.

luggage bins, interior walls or seat structures [56].The improved understanding of weave layer alignment influence on surface topography may allow more optimal material selection and manufacture by better controlling the surface smoothness and reducing the need for post-forming coating, improving weight and durability. Moreover, the insights provided by the characterisation of strain and topography for manufacture can be further complemented by a simultaneous investigation of damage.

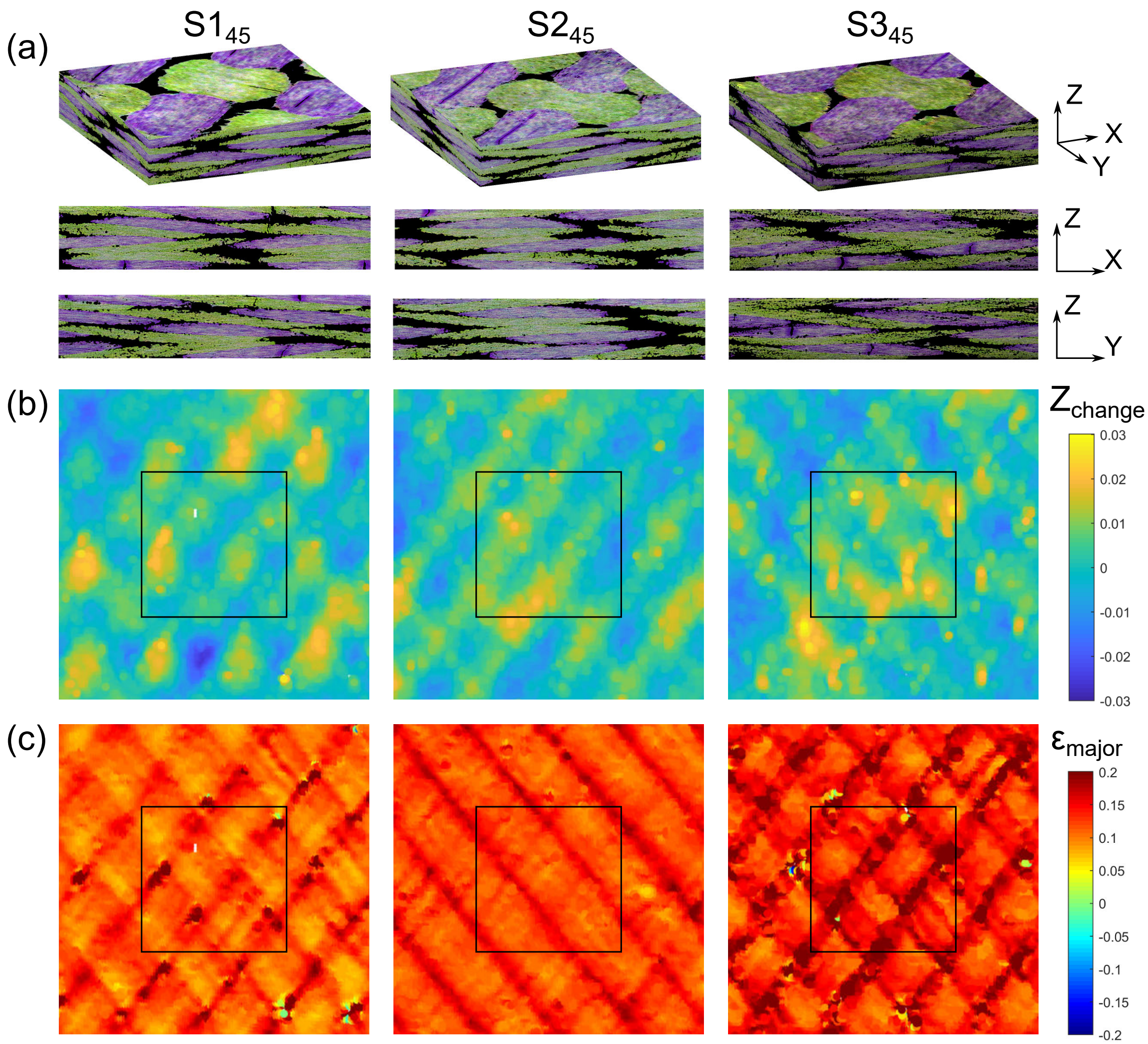

Figure 10: Off-axis 45° orientation, (a) fibre orientation architecture for specimens $S1_{45}$, $S2_{45}$, and $S3_{45}$ showing volumetric view (4.2 x 4.2 x 1 mm), XZ, and YZ cross-sections (resin masked to black) of μCT volume, (b) surface topography (Z_{change}) from DIC, (c) major principal strain (ϵ_{major}) for region corresponding to topography and architecture; black box in (b) and (c) shows location of corresponding μCT volume. Additional strain plots in Supplementary figure 4.

3.4. Damage development

Damage was identified in μCT images of specimens in the form of matrix cracks. These cracks mainly occur within fibre tows and are aligned with the fibre direction. Inspection of the two middle layers shows that cracks infrequently occur for 0° and 15° specimens, see Figure 11a,b, and when they do, they are generally short. Meanwhile, cracks for 30° and 45° specimens, see Figure 11c,d, are more common and substantially longer and extend to tow edges. Cracks for 30° specimens are primarily in the 30° orientation, while for the 45° specimens, they tend to be in one primary orientation. It is

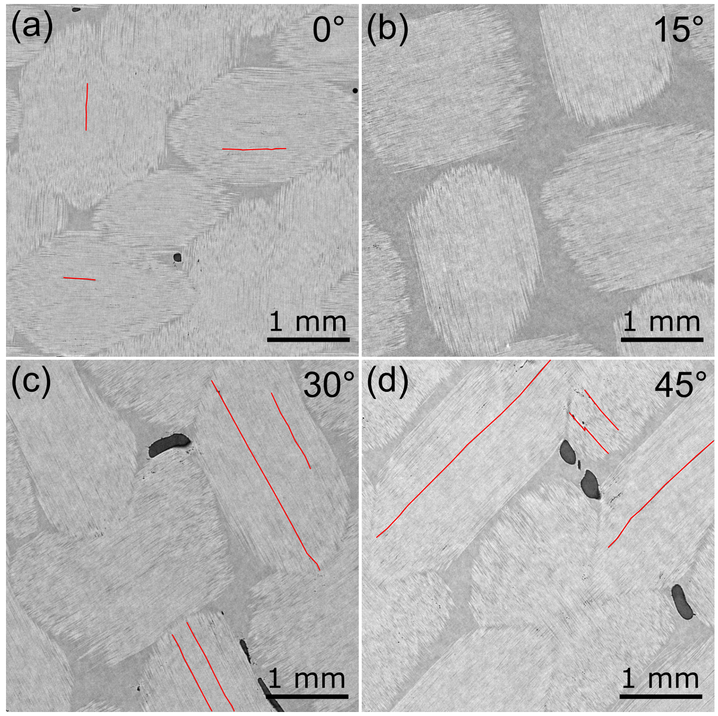

Figure 11: Internal tow matrix cracking for representative X-Y tomogram images of, (a) 0°, (b) 15°, (c) 30°, and (d) 45° specimens, showing more frequent and longer cracks for 30° and 45° specimens. Cracks identified via grey level threshold and then manually traced in red for visualisation clarity (see also Figure 12).

likely that these cracks are a consequence of intra-tow shear deformation. This intra-tow deformation is further evidenced by surface DIC, which can be matched with underlying cracks beneath the paint layer that are often not visible on the surface. This is illustrated in Figure 12a for a 30° specimen, where the μCT tomogram shows frequent cracking, primarily in the 30° off-axis tows. The corresponding region of surface DIC in Figure 12b shows high strain in the matrix region between tows, but also in regions corresponding to tow cracks in the 30° and occasionally in the 60° tows. The crack width is often insufficient to break the surface paint, but the shearing deformation is sufficient to detect with DIC. These experimental results are a clear demonstration of the existence of intra-tow deformation for off-axis loading of woven composites, in addition to the more widely reported inter-tow deformation, [12, 14, 27]. Without the benefit of high-resolution DIC ideally coupled with μCT 3D image analysis, intra-tow deformation is hard to detect and classify. Our results now enable better interpretation of these DIC features, even for test setups without the benefit of the underlying x-ray μCT imaging of internal damage.

The μCT based analysis also appears to indicate a lesser degree of damage, specifically intra-tow cracking, compared to studies of woven thermoset composites [10, 13]. Similarly, evidence of differences in local damage induced by variations in layer alignment is not found, as has previously

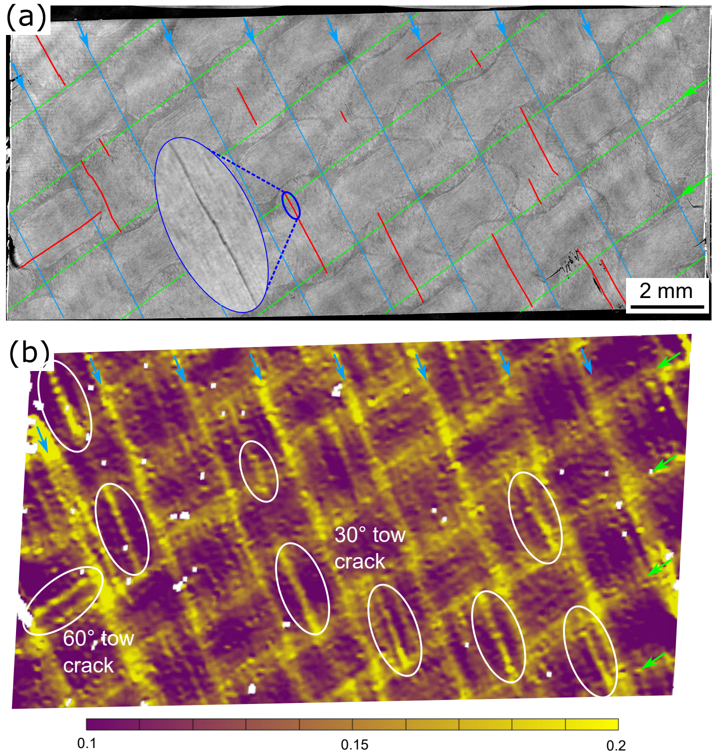

Figure 12: Surface weave layer cracks correspondence with strain for a 30° specimen, (a) beneath surface paint tomogram image with cracks marked in red for clarity, and (b) DIC of the major principal strain of the corresponding region showing the location of high inter-tow strain (blue and green arrows) and intra-tow cracks. Note, distortion of the matching DIC region is due to deformation under load; fine 3 pixel steps and high contrast colour map used to better expose cracks.

been observed for thermosets [40, 41]. Despite architectural variations inducing different local strain and topographical deformation, the deformation is often insufficient to induce damage in the ductile PEEK matrix, as may be the case for more brittle thermosets. The approach described in this paper can be used for similar investigations of off-axis tensile loading and failure behaviour of woven composites with different fibre reinforcement and ductile thermoplastic matrices.

The coupled DIC and μCT approach is also helpful for developing and refining finite element models for mesoscale deformation and damage progression analysis. Segmented μCT microstructure provides authentic geometry, which improves the accuracy of the model. Models based on the scanned architecture, named digital material twins, are of increasing interest [6, 8, 57]. Moreover, the DIC results would allow validation and optimisation of these models, using the measured displacement around the selected volume as boundary conditions and the heterogeneity of the mesoscale strain and topography for behaviour comparison. Therefore, compared to experimental findings, failure criteria can be tested numerically on the authentic architecture and the progressive mesoscale strain and topographical response. Once developed for a representative volume, the modelling approach can be repeated for the different layer-alignments to use statistical or multiscale approaches for macroscale approximations and engineering design criteria. Hence, there is significant potential for using this experimental approach in conjunction with numerical models for enhanced understanding of failure behaviour.

4. Conclusions

The close link between internal weave architecture and surface topography and strain has been demonstrated for both on- and off-axis extension. This relationship increases the value of the mesoscale surface data captured with DIC, as it can signal features of the internal structure of woven composites. These insights may help improve understanding of local behaviour during testing, as inputs for refining mesoscale weave simulations and as criteria for quality control comparison during manufacture. Specific insights for both tensile properties and mesoscale behaviour are as follows for the tested plain weave C/PEEK composite:

- Tensile properties changed significantly for an increasingly off-axis direction with decreasing stress (factor of 2), elastic modulus (factor of 4), increasing absorbed energy (5 times) and strain to failure (12 times).
- A fibre failure metric from surface fibre strain is shown to be inadequate for failure prediction in scenarios of high shear strain, as is the case for the off-axis loading.
- Fibre reorientation within the composite increases with off-axis direction, up to 15° reorientation during bias extension observed with DIC. μCT images show a $\sim$50% recovery of fibre reorientation after unloading for all off-axis specimens.
- Nested alignment of the top two weave layers results in continuous topographical ridges and valleys, while aligned layers have distinct topographical peaks. Balanced layers can also produce distinct topographical peaks, but their height is less than aligned layers for on-axis loading.
- Increased topographical height is seen with off-axis specimens due to greater fibre reorientation, with mean peak to valley heights > 30 μm compared to 18.7 μm for on-axis.
- The highest strain occurs in transverse tows for on-axis specimens and increasingly in matrix rich inter-tow regions with greater off-axis loading.
- Intra-tow matrix cracks align with the fibre direction, with increasing crack lengths evident in the 30° and 45° specimens. Furthermore, the 3D visualisation provided by μCT imaging of cracks near the surface can be matched with surface strain, showing that they contribute to deformation

during off-axis extension. This illustrates the benefit of combining DIC and μCT observations to understand deformation and damage mechanisms.

- Coupled DIC and μCT results have the potential to improve off-axis deformation and damage simulations by using accurate 3D architecture and validating simulated behaviour against measured mesoscale strain and topography.

5. Acknowledgements

This project was in part conducted within the ARC Training Centre for Automated Manufacture of Advanced Composites (IC160100040), supported by the Commonwealth of Australia under the Australian Research Council's Industrial Transformation Research Program. The support of the Australian Government Research Training Program (RTP) Scholarship (John Holmes) is also acknowledged. The authors would also like to express their sincere thanks to the personnel involved with the ANU X-ray Computed Tomography laboratory (CTLab) for technical support and the ANU Supercomputer Facility and National Computational Infrastructure (NCI) for their generous allocation of computing time.

6. Data availability

The primary raw/processed data required to support these findings have been included in this article and supplementary materials. Additional data, such as μCT slices, is available from the corresponding author upon reasonable request.

References

[1] Zheng B, Gao X, Li M, Deng T, Huang Z, Zhou H, et al. Formability and Failure Mechanisms of Woven CF/PEEK Composite Sheet in Solid-State Thermoforming. Polymers 2019;11:966.

[2] Long AC, Clifford MJ. Composite forming mechanisms and materials characterisation. In: Long AC, editor. Composites Forming Technologies; chap. 1. Elsevier Ltd. ISBN 9781845690335; 2007, p. 1–21.

[3] Deng T, Zhang W, Jiang W, Zhou H, Huang Z, Peng X, et al. A hybrid lamination model for simulation of woven fabric reinforced thermoplastic composites solid-state thermo-stamping. Materials & Design 2020;200:109419.

[4] Pan B. Digital image correlation for surface deformation measurement: historical developments, recent advances and future goals. Measurement Science and Technology 2018;29:1–32.

[5] Reu PL, Toussaint E, Jones E, Bruck HA, Iadicola M, Balcaen R, et al. DIC Challenge: Developing Images and Guidelines for Evaluating Accuracy and Resolution of 2D Analyses. Experimental Mechanics 2018;58:1067–99.

[6] Naresh K, Khan KA, Umer R, Cantwell WJ. The use of X-ray computed tomography for design and process modeling of aerospace composites: A review. Materials and Design 2020;190:108553.

[7] Böhm R, Stiller J, Behnisch T, Zscheyge M, Protz R, Radloff S, et al. A quantitative comparison of the capabilities of in situ computed tomography and conventional computed tomography for damage analysis of composites. Composites Science and Technology 2015;110:62–8.

[8] Garcea SC, Wang Y, Withers PJ. X-ray computed tomography of polymer composites. Composites Science and Technology 2018;156:305–19.

[9] Huang J, Zhao Q, Feng Y, Zhou H, Sun F, Wang K, et al. Effect of Microcracks on the Tensile Properties of 3D Woven Composites. Coatings 2021;11:794.

[10] Zhao D, Wang W, Hou Z. Tensile Initial Damage and Final Failure Behaviors of Glass Plain-weave Fabric Composites in On- and Off-axis Directions. Fibers and Polymers 2019;20:147–57.

[11] Wang L, Zhao B, Wu J, Chen C, Zhou K. Experimental and numerical investigation on mechanical behaviors of woven fabric composites under off-axial loading. International Journal of Mechanical Sciences 2018;141:157–67.

[12] Koohbor B, Ravindran S, Kidane A. Meso-scale study of non-linear tensile response and fiber trellising mechanisms in woven composites. Journal of Reinforced Plastics and Composites 2016;35:986–95.

[13] Zhou G, Sun Q, Li D, Meng Z, Peng Y, Zeng D, et al. Effects of fabric architectures on mechanical and damage behaviors in carbon/epoxy woven composites under multiaxial stress states. Polymer Testing 2020;90:106657.

[14] Yang J, Yang X, Zhu H, Shi D, Chen X, Qi H. The effect of off-axis angles on the mesoscale deformation response and failure behavior of an orthotropic textile carbon-epoxy composite. Composite Structures 2018;206:952–9.

[15] Mostafa NH, Ismarrubie ZN, Sapuan SM, Sultan MT. Effect of fabric biaxial prestress on the fatigue of woven E-glass/polyester composites. Materials and Design 2016;92:579–89.

[16] Ivanov SG, Beyens D, Gorbatikh L, Lomov SV. Damage development in woven carbon fibre thermoplastic laminates with PPS and PEEK matrices: A comparative study. Journal of Composite Materials 2017;51:637–47.

[17] Hufenbach W, Gude M, Böhm R, Zscheyge M. The effect of temperature on mechanical properties and failure behaviour of hybrid yarn textile-reinforced thermoplastics. Materials & Design 2011;32:4278–88.

[18] Hu J, Gao C, He S, Chen W, Li Y, Zhao B, et al. Effects of on-axis and off-axis tension on uniaxial mechanical properties of plain woven fabrics for inflated structures. Composite Structures 2017;171:92–9.

[19] Cai D, Wang X, Deng J, Zhou G. Coupling coefficients of glass/epoxy laminates under off-axis tensile conditions: Experimental verification. Polymer Testing 2017;63:334–41.

[20] Hernandez TP, Mills AR, Yazdani Nezhad H. Shear driven deformation and damage mechanisms in High-performance carbon Fibre-reinforced thermoplastic and toughened thermoset composites subjected to high strain loading. Composite Structures 2021;261:113289.

[21] Vieille B, Chabchoub M, Gautrelet C. Influence of matrix ductility and toughness on strain energy release rate and failure behavior of woven-ply reinforced thermoplastic structures at high temperature. Composites Part B: Engineering 2018;132:125–40.

[22] Foti F, Pannier Y, Gigliotti M. High temperature fatigue of carbon/polyimide 8-harness satin woven composites. Part II: Environmental effects. Composite Structures 2020;244:112251.

[23] Holmes J, Hafiz Y, Stachurski Z, Das R, Kalyanasundaram S. Surface topography evolution of woven thermoplastic composites under deformation. Composites Part B: Engineering 2020;188:107880.

[24] Doitrand A, Fagiano C, Chiaruttini V, Leroy FH, Mavel A, Hirsekorn M. Experimental characterization and numerical modeling of damage at the mesoscopic scale of woven polymer matrix composites under quasi-static tensile loading. Composites Science and Technology 2015;119:1–11.

[25] Sun G, Kong X, Wang Z, Luo Q, Li Q. Experimental investigation into stamping of woven CF/PP laminates: Influences of molding temperature on thermal, mesoscopic and macroscopic properties. Composite Structures 2021;263:113507.

[26] Jebri L, Abbassi F, Demiral M, Soula M, Ahmad F. Experimental and numerical analysis of progressive damage and failure behavior of carbon Woven-PPS. Composite Structures 2020;243:112234.

[27] Koohbor B, Ravindran S, Kidane A. A multiscale experimental approach for correlating global and local deformation response in woven composites. Composite Structures 2018;194:328–34.

[28] Ivanov DS, Lomov SV, Bogdanovich AE, Karahan M, Verpoest I. A comparative study of tensile properties of non-crimp 3D orthogonal weave and multi-layer plain weave E-glass composites. Part 2: Comprehensive experimental results. Composites Part A: Applied Science and Manufacturing 2009;40:1144–57.

[29] Holmes J, Vlandis G, Stachurski Z, Das R, Compston P. Failure behaviour in woven thermoplastic composites subjected to various deformation modes. Composites Part A: Applied Science and Manufacturing 2021;146:106410.

[30] Boufaida Z, Boisse J, André S, Farge L. Mesoscopic strain field analysis in a woven composite using a spectral solver and 3D-DIC measurements. Composite Structures 2017;160:604–12.

[31] Rossol MN, Rajan VP, Zok FW. Effects of weave architecture on mechanical response of 2D ceramic composites. Composites Part A: Applied Science and Manufacturing 2015;74:141–52.

[32] Doitrand A, Fagiano C, Leroy FH, Mavel A, Hirsekorn M. On the influence of fabric layer shifts on the strain distributions in a multi-layer woven composite. Composite Structures 2016;145:15–25.

[33] Daggumati S, Van Paepegem W, Degrieck J, Praet T, Verhegghe B, Xu J, et al. Local strain in a 5-harness satin weave composite under static tension: Part II – Meso-FE analysis. Composites Science and Technology 2011;71:1217–24.

[34] Espadas-Escalante JJ, van Dijk NP, Isaksson P. The effect of free-edges and layer shifting on intralaminar and interlaminar stresses in woven composites. Composite Structures 2018;185:212–20.

[35] Shady E, Gowayed Y. Interlaminar shear stress distribution between nested layers of plain weave composites. Polymer Composites 2010;31:1838–45.

[36] Kubo G, Matsuda T, Sato Y. A novel basic cell modeling method for elastic-viscoplastic homogenization analysis of plain-woven laminates with nesting. International Journal of Mechanical Sciences 2018;146-147:497–506.

[37] Huang HS. Influence of phase shift on the responses of woven laminated composites. Composite Structures 2015;130:143–54.

[38] Varandas LF, Catalanotti G, Melro AR, Falzon BG. On the importance of nesting considerations for accurate computational damage modelling in 2D woven composite materials. Computational Materials Science 2020;172:109323.

[39] Matveev MY, Long AC, Brown LP, Jones IA. Effects of layer shift and yarn path variability on mechanical properties of a twill weave composite. Journal of Composite Materials 2017;51:913–25.

[40] Cai D, Tang J, Zhou G, Wang X, Li C, Silberschmidt VV. Failure analysis of plain woven glass/epoxy laminates: Comparison of off-axis and biaxial tension loadings. Polymer Testing 2017;60:307–20.

[41] Olave M, Vara I, Husabiaga H, Aretxabaleta L, Lomov SV, Vandepitte D. Nesting effect on the mode I fracture toughness of woven laminates. Composites Part A: Applied Science and Manufacturing 2015;74:166–73.

[42] Daggumati S, De Baere I, Van Paepegem W, Degrieck J, Xu J, Lomov S, et al. Local damage in a 5-harness satin weave composite under static tension: Part I – Experimental analysis. Composites Science and Technology 2010;70:1926–33.

[43] Yousaf Z, Withers P, Potluri P. Compaction, nesting and image based permeability analysis of multi-layer dry preforms by computed tomography (CT). Composite Structures 2021;263:113676.

[44] Zeng X, Endruweit A, Brown LP, Long AC. Numerical prediction of in-plane permeability for multilayer woven fabrics with manufacture-induced deformation. Composites Part A: Applied Science and Manufacturing 2015;77:266–74.

[45] Yang B, Wang S, Wang Y. Effect of Nesting in Laminates on the Through-Thickness Permeability of Woven Fabrics. Applied Composite Materials 2018;25:1237–53.

[46] Malpot A, Touchard F, Bergamo S. An investigation of the influence of moisture on fatigue damage mechanisms in a woven glass-fibre-reinforced PA66 composite using acoustic emission and infrared thermography. Composites Part B: Engineering 2017;130:11–20.

[47] Nikforooz M, Montesano J, Golzar M, Shokrieh MM. Assessment of failure toughening mechanisms in continuous glass fiber thermoplastic laminates subjected to cyclic loading. Composites Part B: Engineering 2019;161:344–56.

[48] Daggumati S, De Baere I, Van Paepegem W, Degrieck J, Xu J, Lomov SV, et al. Fatigue and post-fatigue stress-strain analysis of a 5-harness satin weave carbon fibre reinforced composite. Composites Science and Technology 2013;74:20–7.

[49] Holmes J, Das R, Stachurski Z, Compston P, Kalyanasundaram S. Development of an S-specimen geometry for shear testing of woven thermoplastic composites. Composites Part B 2020;203:108485.

[50] Sommacal S, Matschinski A, Drechsler K, Compston P. Characterisation of void and fiber distribution in 3D printed carbon-fiber/PEEK using X-ray computed tomography. Composites Part A: Applied Science and Manufacturing 2021;149:106487.

[51] Myers GR, Kingston AM, Latham SJ, Recur B, Li T, Turner ML, et al. Rapidly converging multigrid reconstruction of cone-beam tomographic data. In: Developments in X-Ray Tomography X; vol. 9967. ISBN 9781510603257; 2016, p. 99671M.

[52] Sheppard A, Latham S, Middleton J, Kingston A, Myers G, Varslot T, et al. Techniques in helical scanning, dynamic imaging and image segmentation for improved quantitative analysis with X-ray micro-CT. Nuclear Instruments and Methods in Physics Research, Section B: Beam Interactions with Materials and Atoms 2014;324:49–56.

[53] Sommacal S, Kingston A, Plöckl M, Matschinski A, Consul P, Saadatfar M, et al. 3d characterisation of carbon fibre reinforced composite microstructure via x-ray computed tomography. In: ICCM22 - 22nd International Conference on Composite Materials. Melbourne (Australien); 2019, p. 1–12.

[54] Püspöki Z, Storath M, Sage D, Unser M. Transforms and Operators for Directional Bioimage Analysis: A Survey. In: Advances in Anatomy Embryology and Cell Biology; vol. 219. ISBN 9783319285498; 2016, p. 69–93.

[55] Davey S, Das R, Cantwell WJ, Kalyanasundaram S. Forming studies of carbon fibre composite sheets in dome forming processes. Composite Structures 2013;97:310–6.

[56] Toray Advanced Composites . Aerospace: Advanced Composite Materials Selector Guide. 2020. URL: `https://www.toraytac.com/products/thermoplastic/reinforced-thermoplastic-laminates`.

[57] Holmes J, Sommacal S, Stachurski Z, Das R, Compston P. Digital image and volume correlation with x-ray micro-computed tomography for deformation and damage characterisation of woven fibre-reinforced composites. Composite Structures 2021;:114775.